ResearchGate

See discussions, stats, and author profiles for this publication at: https://www.researchgate.net/publication/276121338

Hybrid Constraints of Pure and Mixed Pixels for Soft-Then-Hard Super-Resolution Mapping With Multiple Shifted Images

Article *in* IEEE Journal of Selected Topics in Applied Earth Observations and Remote Sensing · May 2015

DOI: 10.1109/JSTARS.2015.2417191

CITATIONS
9

READS
121

5 authors, including:

Yong Ge
State Key Laboratory of Resources and Envir…
82 PUBLICATIONS **589** CITATIONS
SEE PROFILE

Gerard Heuvelink
Wageningen University & Research
301 PUBLICATIONS **6,276** CITATIONS
SEE PROFILE

Hu Jianlong
Shanxi University
5 PUBLICATIONS **24** CITATIONS
SEE PROFILE

Yu Jiang
State Key Laboratory of Resources and Envir…
3 PUBLICATIONS **30** CITATIONS
SEE PROFILE

Some of the authors of this publication are also working on these related projects:

Project
Model-based Bayesian geostatistics for multi-scale mapping of soil and agronomic variables View project

Project
UncertWeb View project

All content following this page was uploaded by Yong Ge on 25 July 2015.

The user has requested enhancement of the downloaded file. All in-text references underlined in blue are added to the original document and are linked to publications on ResearchGate, letting you access and read them immediately.

Hybrid Constraints of Pure and Mixed Pixels for Soft-Then-Hard Super-Resolution Mapping With Multiple Shifted Images

Yuehong Chen, Yong Ge, *Member, IEEE*, Gerard B. M. Heuvelink, Jianlong Hu, and Yu Jiang

***Abstract*—Multiple shifted images (MSIs) have been widely applied to many super-resolution mapping (SRM) approaches to improve the accuracy of fine-scale land-cover maps. Most SRM methods with MSIs involve two processes: subpixel sharpening and class allocation. Complementary information from the MSIs has been successfully adopted to produce soft attribute values of subpixels during the subpixel sharpening process. Such information, however, is not used in the second process of class allocation. In this paper, a new class-allocation algorithm, named "hybrid constraints of pure and mixed pixels" (HCPMP), is proposed to allocate land-cover classes to subpixels using MSIs. HCPMP first determines the classes of subpixels that overlap with the pure pixels of auxiliary images in MSIs, after which the remaining subpixels are classified using information derived from the mixed pixels of the base image in MSIs. An artificial image and two remote sensing images were used to evaluate the performance of the proposed HCPMP algorithm. The experimental results demonstrate that HCPMP successfully applied MSIs to produce SRM maps that are visually closer to the reference images and that have greater accuracy than five existing class-allocation algorithms. Especially, it can produce more accurate SRM maps for high-resolution land-cover classes than low-resolution cases. The algorithm takes slightly less runtime than class allocation using linear optimization techniques. Hence, HCPMP provides a valuable new solution for class allocation in SRM using auxiliary data from MSIs.**

***Index Terms*—Hybrid constraints, multiple shifted images (MSIs), remotely sensed imagery, super-resolution mapping (SRM).**

Manuscript received August 07, 2014; revised March 18, 2015; accepted March 23, 2015. Date of publication April 13, 2015; date of current version July 20, 2015. This work was supported in part by the National Natural Science Foundation of China under Grant 41471296 and in part by the Key Technologies Research and Development Program of China (2012BAH33B01). *(Corresponding author: Yong Ge.)*

Y. Chen and Y. Jiang are with the State Key Laboratory of Resources and Environmental Information System, Institute of Geographical Sciences and Natural Resources Research, University of Chinese Academy of Sciences, Beijing 100101, China (e-mail: chenyh@lreis.ac.cn; jiangy@lreis.ac.cn).

Y. Ge is with the State Key Laboratory of Resources and Environmental Information System, Institute of Geographical Sciences and Natural Resources Research, University of Chinese Academy of Sciences, Beijing 100101, China and also with Jiangsu Center for Collaborative Innovation in Geographical Information Resource Development and Application, Nanjing 210023, China (e-mail: gey@lreis.ac.cn).

G. B. M. Heuvelink is with the Soil Geography and Landscape Group, Wageningen University, Wageningen 6708 PB, The Netherlands (e-mail: gerard.heuvelink@wur.nl).

J. Hu is with the School of Computer and Information Technology, Shanxi University, Taiyuan 030006, China (e-mail: weilong@sxu.edu.cn).

Color versions of one or more of the figures in this paper are available online at http://ieeexplore.ieee.org.

Digital Object Identifier 10.1109/JSTARS.2015.2417191

I. Introduction

LAND COVER is a fundamental variable in many scientific investigations and operational applications such as land-cover change, ecology, and hydrology [1], [2]. Extraction of land-cover maps from remote sensing images is typically accomplished by classification. However, the presence of mixed pixels in remote sensing images will often lead to an inaccurate representation of land-cover by traditional hard and soft classification techniques [3], [4]. Super-resolution mapping (SRM), also termed as subpixel mapping, was proposed by Atkinson [5] to provide a solution to the mixed pixel problem in classification. SRM transforms the output (i.e., fraction images) of soft classification into a hard classification map with a finer spatial resolution than the input images [6].

In past decades, various SRM approaches have been developed, including the Hopfield neural network [7], linear optimization techniques [8], genetic algorithms [9], the pixel-swapping algorithm [10], back-propagation neural networks [11], [12], Markov random fields [13]–[16], subpixel/pixel spatial attraction models [17]–[19], the geometric method [20], the vectorial boundary-based method [21], geostatistical methods [22], [23], artificial intelligence-based methods [24]–[27], and radial basis functions [28]. These approaches have achieved relatively satisfactory performance in several applications, such as waterline mapping [29], urban tree identification [13], enhancement of the landscape pattern index [30], land-cover change detection [31], urban building extraction [32], lake area estimation [33], and floodplain inundation mapping [34].

Most traditional SRM approaches are underdetermined in which there may be multiple plausible solutions if fraction images from only a single image are applied to predict the spatial distribution of subpixels within a mixed pixel [6], [23], [35]–[38]. Such an underdetermined process leads to ambiguity and uncertainty in the SRM results, which limits the accuracy of SRM maps. One solution to this problem is to use auxiliary data, such as prior knowledge [10], [23], [32], [39]–[42], panchromatic images [43]–[45], land-line digital vector data [46], light detection and ranging (LIDAR) data [47], fused images [48], digital elevation models [29], [34], class membership contours [49], [50], or multiple shifted images (MSIs) [35]–[37], [51]–[53] to eliminate ambiguity and reduce uncertainty. Compared with other auxiliary datasets, MSIs are relatively easy to obtain by camera movements in the same area [36]. As a result, MSIs have been widely applied to SRM to

1939-1404 © 2015 IEEE. Personal use is permitted, but republication/redistribution requires IEEE permission.
See http://www.ieee.org/publications_standards/publications/rights/index.html for more information.

improve the accuracy of land-cover maps at the subpixel scale [6], [23], [35]–[37].

The multiobservation capability of observation satellites enables us to readily obtain MSIs covering the same area. MSIs include two categories: 1) multitemporal images, which are generated when satellites observe the same area at different times (e.g., the moderate-resolution imaging spectroradiometer (MODIS) covers the entire Earth every 1–2 days); and 2) multiangle images, which are acquired when satellites capture the same area from different angles using multiple sensors (e.g., the multiangle imaging spectroradiometer (MISR) consists of nine separate digital cameras that gather data in various directions). These images are usually not identical but are shifted by several subpixels owing to slight orbit-translation and the Earth's rotation [37]. Thus, these multiobservation satellite sensors can provide MSIs conveniently. Ling *et al.* [37] first proposed to consider MSIs as new constraints in the energy function of a Hopfield neural network for improving the accuracy of SRM maps. Wang and Shi [52] used MSIs in image interpolation to enhance the accuracy of SRM maps, while Wang and Wang [51] incorporated multiple spectral constraints from the MSIs into a Markov random field. Xu *et al.* [53] improved the spatial attraction model with MSIs (SAM_MSI), and Wang *et al.* [35] enhanced the accuracy of indicator cokriging by fusing conditional probability maps from MSIs (ICK_MSI). Xu *et al.* [36] considered SRM as a regularization issue based on the maximum *a posteriori* with MSIs (MAP_MSI). All these methods had improved performance when compared with SRM maps generated with a single input image. They can be regarded as soft-then-hard SRM (STHSRM), which was first summarized by Wang *et al.* [54]. Note that STHSRM is not only suitable for MSIs but also for a single input image. STHSRM contains two processes: 1) subpixel sharpening, in which soft attribute values of each subpixel for all land-cover classes are estimated; and 2) class allocation, whereby hard attribute values (i.e., land-cover labels) of subpixels within a mixed pixel are allocated according to the soft attribute values and fraction images [54]. However, the STHSRM methods with MSIs discussed above applied the complementary information encapsulated in the MSIs to the first process only (i.e., subpixel sharpening). The second process of class allocation did not use the complementary information, which may result in limited SRM accuracy improvement.

To take full advantage of MSIs in the process of class allocation, this paper proposes a new class allocation method for STHSRM with MSIs, which allocates the classes to subpixels using hybrid constraints of pure and mixed pixels (HCPMP). The new HCPMP algorithm creates hybrid constraints from both the mixed pixels of a base image and the pure pixels of the auxiliary images in MSIs. It first determines the classes of subpixels that overlap with the pure pixels of auxiliary images, after which the remaining subpixels are classified using information derived from the mixed pixels of the base image. The base image, which can be any one image of MSIs, is considered as the benchmark of spatial reference used to generate land-cover maps at subpixel scale. Currently, five class-allocation algorithms are implemented [54], including direct hardening (DH) [7], [36], [55], units of subpixel (UOS) [22], highest

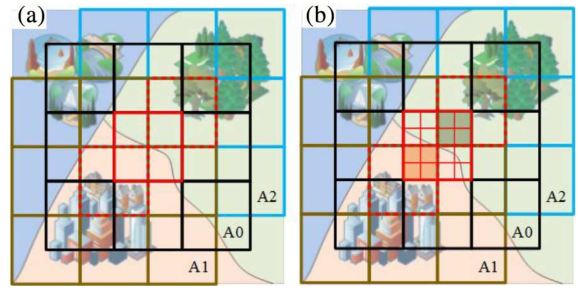

Fig. 1. Super-resolution mapping with MSIs (see main text for further explanation). (a) A region partially covered by three MSIs. (b) The central mixed pixel of image A_0 is overlapped by the pure pixels of other MSIs.

attribute values first (HAVF) [17], units of class (UOC) [54], and linear optimization techniques (LOT) [8]. Compared with the five existing class-allocation algorithms, the HCPMP algorithm has several characteristics and advantages: 1) it can make use of auxiliary images in both subpixel sharpening and class-allocation processes to improve SRM results; 2) the accuracy of SRM may increase, especially for high-resolution land-cover classes, as the uncertainty in the class-allocation process can be reduced using the constraints imposed by pure pixels from the auxiliary images; and 3) compared with LOT, the computational efficiency may be increased as the number of subpixels that need to assign land-cover classes decreases due to the pure pixels in the auxiliary images.

For comparison of the proposed HCPMP algorithm with existing algorithms, three representative subpixel sharpening algorithms (i.e., SAM_MSI, ICK_MSI, and MAP_MSI) are first applied to estimate soft attribute values of subpixels. Next, five existing class-allocation algorithms and the proposed method are employed to determine the land-cover class of each subpixel. An artificial image and two remote sensing images are used to evaluate the performance of HCPMP.

The remainder of this paper is organized as follows. Section II presents the background of STHSRM using MSIs. Section III introduces the proposed HCPMP. Results for remote sensing images are provided in Section IV and discussed in Section V. Finally, conclusion is drawn in Section VI.

II. Background

A. Basic Principles of STHSRM With MSIs

Most STHSRM with MSI approaches estimate the spatial locations of subpixels within a mixed pixel through the subpixel sharpening and class-allocation processes mentioned in Section I. Fig. 1 illustrates the basic idea of SRM with MSIs. Fig. 1(a) shows that there are three land-cover classes—water, forest, and buildings—within the region partially covered by three mutually shifted images—A_0, A_1, and A_2, each of which comprises 3×3 pixels. A_0 is considered as the base image, while the other two are auxiliary (or shifted) images with slight diagonal shift (i.e., one half-pixel) relative to A_0. Given a scale factor $S = 4$, each pixel can be divided into 4×4 smaller subpixels, as shown in the central pixel of A_0 of Fig. 1(b). STHSRM with MSIs approaches first estimate soft attribute values of the 16 subpixels; the classes of these subpixels are then allocated in terms of the estimated soft attribute values and fraction constraints from the base image A_0. Fig. 1(b) shows that the central pixel in auxiliary image A_1 is a pure pixel, covering the four subpixels in the lower left of the central mixed pixel in A_0. The pure pixel of A_1 thus indicates that these four subpixels should be labeled as buildings. Similar to the central pixel in A_1, the central pixel in A_2, which is a pure pixel with the land-cover label of forest, covers four subpixels in the upper right of the central mixed pixel in A_0. It indicates that the four upper-right subpixels of the central pixel of A_0 should be labeled as forest. In this way, MSIs provide relevant information to improve SRM and increase accuracy of land-cover maps at the subpixel scale [35]–[37], [51]–[53].

As the subpixel sharpening and class-allocation processes of STHSRM with MSIs are important to produce land-cover maps, we briefly describe these processes in the following sections.

B. Subpixel Sharpening

Subpixel sharpening disaggregates coarse fraction images into fine soft attribute values of subpixels [54]. Pixels in coarse images are first divided into fine subpixels for a given scale factor, and then, the soft attribute value of each subpixel that belongs to each land-cover class is estimated. This process can be accomplished by many approaches under the assumption of spatial dependence [5], [54]. When fraction images are derived from a single image, the soft attribute values of subpixels are estimated from the single image, whereas in case of fraction images derived from MSIs, the soft attribute values are obtained by fusing the subpixel sharpening results from each of the MSIs, using approaches such as SAM_MSI [53], ICK_MSI [35], and MAP_MSI [36]. SAM_MSI integrates spatial attractions from a base image and auxiliary images into weighted spatial attractions, which are considered as soft attribute values of subpixels. SAM_MSI inherits the advantages of the original spatial attraction model, which is considered as an efficient approach [18], [27] because it is a straightforward one-pass process with simple rules [17]. ICK_MSI, based on geostatistics, first computes a conditional probability map from each coarse image of the MSIs; these probability maps are then averaged as soft attribute values of subpixels [35]. ICK_MSI allows easy integration of fine sample data without any iterative process [35]. MAP_MSI, first presented by Xu *et al.* [36], transforms STHSRM with MSIs into a regularization problem with the maximum *a posteriori* model, and the posteriori probabilities are considered as soft attribute values of the subpixels [36]. Recently, this method has been improved in adaptive parameter selection [56] and the reduction of spectral unmixing error [55]. The three subpixel sharpening algorithms have demonstrated their usefulness in practical situations, and thus, they are used here to estimate the soft attribute values of subpixels.

C. Class-Allocation Algorithms

Class allocation converts the fine soft attribute values of subpixels derived from subpixel sharpening to a hard classified map. In class allocation, the number of subpixels for each class should first be determined according to fraction images and the given scale factor. The land-cover class of each subpixel is then allocated according to the results of subpixel sharpening. Note that when MSIs are applied, the number of subpixels is calculated according to fraction images from the base image. DH was originally applied to Hopfield neural network-based SRM [7], and subsequently, to back-propagation neural network-based approaches [11], [12], [57]. Both UOS and HAVF assign land-cover classes to subpixels in a sequence, while satisfying the coherence constraint that the number of subpixels for each class within a mixed pixel should be consistent with the fraction images. UOS proceeds along a typically predefined visiting path (S^2 subpixels, where S is the scale factor) that determines the order of visited subpixels within a pixel, while HAVF performs along the descending order of all soft attribute values ($C \times S^2$, where C is the number of land-cover classes). UOC, proposed by Wang *et al.* [54], is an advanced class-allocation algorithm that takes intraclass spatial dependence into account. Typically, UOC allocates labels to subpixels according to a visiting order of land-cover classes that can be determined by Moran's I. Verhoeye and De Wulf [8] first applied LOT to the class-allocation process.

DH does not guarantee the coherence constraint and may produce overly smooth results [54]. It, however, may reduce the spectral unmixing error of real remote sensing images [55]. UOS may produce results with a salt-and-pepper effect if the visiting order of subpixels is not appropriate [39]. HAVF and UOC typically generate results with almost the same accuracy, which is generally higher than DH and UOS. UOC is more efficient than HAVF due to fewer comparisons of soft attribute values in UOC [54]. Compared with DH, UOS, HAVF and UOC, LOT usually generate the highest SRM map accuracy, likely due to the fact that it involves many iterations in search for the optimal land-cover classes of subpixels. LOT, however, needs significantly more runtime than the other four class-allocation algorithms [54]. Note that UOC may produce results with slightly higher accuracy than LOT if the visiting order of land-cover classes is set appropriately, as shown in [54]. Although all five existing class-allocation algorithms have advantages and disadvantages, none of them use the pure pixels in auxiliary images to increase the accuracy of SRM results.

III. HCPMP Algorithm

Based on the brief description of the five existing class-allocation algorithms given in the previous section, it is clear that they only use soft attribute values and coarse fraction images from a base image to estimate the spatial locations of subpixels. Complementary information in auxiliary images is ignored in the process of class allocation. Although the complementary information may produce more accurate soft attribute values in the subpixel sharpening process, the resulting accuracy of the SRM map may still be modest, especially when using a large zoom scale [35]. It is, therefore, attractive to also apply auxiliary images to the class-allocation process to further reduce the uncertainty in SRM.

As shown in Fig. 1(b), the complementary information of the two central pure pixels in the auxiliary images (i.e., images A_1 and A_2) is useful to decrease the uncertainty in SRM. When the two pure pixels are applied to class allocation, the land-cover classes of the eight subpixels within the central mixed pixel of base image A_0 can be determined directly. The uncertainty of the eight subpixels is completely removed, leading to a reduction in the total SRM uncertainty. The eight remaining subpixels can then be allocated to land-cover classes according to the soft attribute values and constraints of the fraction images from a base image. The HCPMP algorithm is based on the above strategy for assigning land-cover classes to subpixels. HCPMP consists of two steps: 1) it first assigns land-cover classes to those subpixels that overlap with the pure pixels of auxiliary images in MSIs; 2) it allocates the remaining subpixels to land-cover classes using the mixed pixels of a base image in MSIs. Both steps are described in detail below.

Suppose that a coarse remote sensing image has m coarse pixels and C land-cover classes. Let $Y = \{Y^{(k)}|k = 1,\ldots,K\}$ be the fraction images derived from the soft classification of coarse MSIs, where K is the number of MSIs. Let image $(Y^{(1)})$ be the base image, while the other images $(\{Y^{(k)}|k = 2,\ldots,K\})$ are the auxiliary (shifted) images in MSIs. Let $Y^{(k)} = (\boldsymbol{y}_{\cdot c}^{(k)})$, $c = 1,\ldots,C$ be fraction images from the kth image of MSIs, where $\boldsymbol{y}_{\cdot c}^{(k)} = \{(y_{i,c}^{(k)})|i = 1,\ldots,m\}$ is the column vector composed of elements $y_{i,c}^{(k)} \in [0, 1]$, denoting the fraction value of coarse pixel i that belongs to land-cover class c. Given the scale factor S, the SRM output is, therefore, a fine-resolution land-cover map X, created by dividing each coarse pixel into $S \times S$ fine pixels (subpixels), where $X = \{x_{j,c}|j = 1,\ldots,M, c = 1,\ldots,C \text{ and } M = m \times S^2\}$ and $x_{j,c} \in \{0, 1\}$ is defined in (1). This indicates that each subpixel should be allocated to a value of one or zero for each land-cover class, where one means that the subpixel belongs to the particular class and zero that it does not. Meanwhile, each subpixel in the SRM map should be allocated to one and only one land-cover class, implying the condition $\sum_{c=1}^{C} x_{j,c} = 1$ for all $j = 1,\ldots,M$

$$x_{j,c} = \begin{cases} 1, & \text{subpixel } j \text{ is classified as class } c \\ 0, & \text{otherwise.} \end{cases} \tag{1}$$

A. *Allocating Classes Using Pure Pixels in Auxiliary Images*

Pure pixels are important in class allocation because subpixels within pure pixels in the base image can be directly assigned the same land-cover class before class allocation and because HCPMP needs pure pixels in auxiliary images to improve the accuracy of SRM maps. Therefore, pure pixels in MSIs should be identified prior to performing the class allocation. Whether a pixel in coarse images is pure can be derived from fraction values of the soft classification. If a pixel is pure, there must be a land-cover class with a fraction value greater than a chosen threshold $\theta \in (0, 1]$. Generally, there are two ways to determine the threshold θ. First, it can be a predefined threshold determined by experts. For example, if $\theta = 0.95$ is identified by experts, then this means that a land-cover class must occupy 95% of the pixel area in order for this pixel to be identified as a pure pixel. The predefined threshold can be set to different values under different conditions. Second, the threshold may be based on the scale factor S. It may be set to $\theta = 1 - 1/S^2$, where $1/S^2$ is the subpixel fraction value. In this case, the pixel is considered pure when the sum of fraction values of other classes is smaller than the fraction value of a single subpixel.

The process of allocating classes to subpixels using pure pixels in auxiliary images includes the following five steps.

Step 1) For mixed pixel i under consideration, the number of subpixels for each class is calculated from the fraction images derived from the base image by

$$N_{i,c} = \mathrm{round}\left(y_{i,c}^{(1)} \times S^2\right) \tag{2}$$

where $N_{i,c}$ is the number of subpixels for class c in pixel i and $\mathrm{round}(\cdot)$ is the operator that rounds its argument toward the closest integer.

Step 2) Using (3) and the criterion of defining pure pixels, identify pure pixels (i.e., $i^{(2)},\ldots,i^{(K)}$) in auxiliary images that may overlap with the mixed pixel i under consideration

$$V_{i^{(k)}} = \mathrm{round}\left(V_{i^{(1)}} + \Delta_k\right) \tag{3}$$

where $V_{i^{(k)}}$ denotes the coordinates of pixel i in the kth image and Δ_k is the shift between the base image and the kth image in the MSIs.

Step 3) For each land-cover class c, remove overlapped pure pixels with the same class using (4). If there is more than one overlapped pure pixel with the same class according to Step 2), the pure pixel with the highest overlapped area less than the fraction of class c within the mixed pixel i is kept for class allocation, and the other overlapped pure pixels are removed. The reason why some overlapped pure pixels in auxiliary images should be removed is that the pure pixel with the highest overlapped area is most suitable for guaranteeing the coherence constraint imposed by fraction images. Therefore, pure pixels in auxiliary images that are in conflict with the coherence constraint should be removed

$$y_{i,c}^{(k)} = \left\{ y_{i,c}^{(k')} \,\middle|\, \lim_{y_{i,c}^{(k')} \to \left(y_{i,c}^{(1)}\right)^{+}} \left(y_{i,c}^{(k')} - y_{i,c}^{(1)}\right) = 0 \right\} \tag{4}$$

where $y_{i,c}^{(k)}$ denotes the kept pure pixel i in the kth image.

Step 4) For each remaining pure pixel $i^{(k)}$ with land-cover class c according to Step 3), the number of subpixels $N_{i^{(k)},c}$ is calculated according to the overlapped area between the pure pixel $i^{(k)}$ and mixed pixel i. The subpixels that overlap with the pure pixel of auxiliary images are allocated to land-cover class c. The number of remaining subpixels within mixed pixel i is updated by $N'_{i,c} = N_{i,c} - N_{i^{(k)},c}$.

Step 5) Repeat the above five steps until all mixed pixels in the base image have been allocated to land-cover classes using pure pixels in auxiliary images.

B. Allocating Classes Using Mixed Pixels in a Base Image

The land-cover class of the remaining subpixels within a mixed pixel of the base image can be determined by any one of the five existing class-allocation algorithms. As LOT is a robust approach [19], [54], it is used here to determine the optimal land-cover classes of remaining subpixels. After the land-cover classes of some subpixels within mixed pixel i have been determined using the overlapped pure pixels in auxiliary images, class allocation for the remaining subpixels is described by the objective function in (5) and constraints given in (6). The objective function aims to maximize the soft attribute values of the remaining subpixels, also subject to class fractions from soft classification

$$\max\text{imize } z = \sum_{c=1}^{C}\sum_{j=1}^{N_i'} x_{j,c} \times p_{j,c} \tag{5}$$

$$\text{subject to} \begin{cases} \sum\limits_{c=1}^{C} x_{j,c} = 1 \\ \sum\limits_{j=1}^{N_i'} x_{j,c} = N_{i,c}' \\ N_i' = \sum\limits_{c=1}^{C} N_{i,c}' \end{cases} \tag{6}$$

where N_i' is the total number of remaining subpixels awaiting class allocation within mixed pixel i and $p_{j,c}$ is the soft attribute value of subpixel j for land-cover class c.

IV. Experiments and Analysis

A. Experimental Design

Three experiments on different images (an artificial image and two remote sensing images) were carried out to evaluate the performance of the proposed HCPMP. The artificial imagery had a relatively simple structure of land-cover patches, which was beneficial to visual evaluation of the performance of the different SRM methods. The two remote sensing images were much more complicated. Three hard-classified land-cover images from each image were considered as reference images, which were considered as the base images in MSIs. The land-cover images were degraded to fraction images to simulate the outputs of soft classification. An advantage of using fraction images obtained by degrading land-cover reference images is that errors in soft classification are avoided which facilitates evaluating the performance of the SRM methods. Fraction images degraded from the fine land-cover image was also a widely used scheme in many SRM studies [16], [35]. For evaluation of the performance of SRM with MSIs, MSIs were generated by shifting reference images. In this way, errors in coregistration and in estimating shifts between the base and auxiliary images were avoided. In each experiment, four shifted images were used, and the subpixel shifts given the scale factor S were $(0,0)$, $(0,S/2)$, $(S/2,0)$, and $(S/2,S/2)$. The four shifted images of each land-cover reference map were degraded into fraction images, which were used as inputs for the subpixel sharpening and class-allocation algorithms. Note that a shift of $(0,0)$ refers to no shift, and hence, these were taken as the base images. In the first experiment on the artificial imagery, three scale factors (4, 6, and 10) were considered. This meant that each land-cover reference map was degraded into coarse fraction images using the three scale factors, and the fraction images were then zoomed in to create fine SRM maps. For the other two experiments with QuickBird and Landsat TM images, a scale factor of 4 was tested.

The three subpixel sharpening algorithms (i.e., SAM_MSI, ICK_MSI, and MAP_MSI) described in Section II were employed to calculate the soft attribute values of subpixels. The five existing class-allocation algorithms described in Section II were used for comparison with the HCPMP algorithm. All six class-allocation algorithms were programmed in Python 2.7 version and were executed on an Intel Core2 Processor (2.93 GHz and 4 GB memory) with the 32-bit Window 7 operating system. For SAM_MSI, the weight was set to $\omega = 0.4$ according to [58]. The parameters in ICK_MSI were the same as those in [35]. For MAP_MSI, a Laplacian model was selected to add prior information owing to its relatively better performance as reported in [36]. To assess the accuracy of each algorithm quantitatively, the adjusted overall accuracy (OA') metric [24] was applied in all three experiments. OA' is identical to the traditional measurement of OA, except that it is calculated for mixed pixels only, which means that OA' was calculated as the total number of correctly classified subpixels divided by the total number of reference subpixels within mixed pixels. The reference subpixels were the corresponding pixels with the same coordinates in the high-resolution reference image. The reference subpixels within all mixed pixels were used as testing samples for accuracy assessment in the three experiments. OA' was used to avoid the influence of pure pixels and concentrate on evaluating SRM method performances for mixed pixels [24], [35].

B. Experiment 1: Artificial Imagery

The size of the artificial image was 240 columns by 240 rows. The image included four land-cover classes (C_1, C_2, C_3, and C_4) as shown in Fig. 2. The reference land-cover map in Fig. 2(a) was shifted to MSIs using four shifts as mentioned in Section IV-A. By applying the three considered scale factors, 4, 6, and 10, they were degraded into fraction images. Fig. 2(b) shows examples of the fraction images degraded from Fig. 2(a), in this case, using scale factor 10.

The fraction images were first used as inputs for the three subpixel sharpening algorithms. The soft attribute values of subpixels from the subpixel sharpening process and fraction images were then used by the five existing class-allocation algorithms and the proposed HCPMP algorithm to recreate land-cover maps with the same spatial resolution as the reference image. The visiting order of the classes (i.e., C_2–C_4–C_1–C_3) for UOC was determined by Moran's I in Table I.

1) SRM Results: Fig. 3 shows SRM results obtained from the coarse fraction images in Fig. 2(b) using scale factor 10. The first column of Fig. 3 shows that DH produced overly smooth maps, while the structures of some land-cover patches failed to be recreated in its results. For example, some small land-cover patches of class C_3 at the image center area failed to be

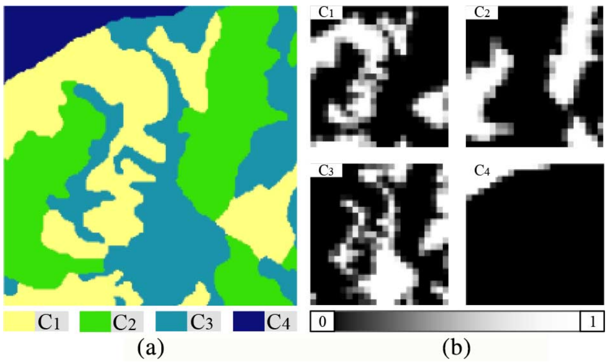

Fig. 2. Experiment on artificial imagery. (a) Reference land-cover map. (b) Fraction images degraded from (a) using scale factor 10.

TABLE I
MORAN'S I OF FOUR CLASSES IN THE ARTIFICIAL IMAGE AT THREE SCALES

S	C_1	C_2	C_3	C_4
4	0.8574	0.9039	0.8280	0.8917
6	0.7970	0.8617	0.7629	0.8330
10	0.6847	0.7807	0.6546	0.7312

recreated and were wrongly classified into class C_1, especially for the map combined with SAM_MSI. Many speckle artifacts occur in the SRM maps created using UOS for class allocation, as shown in the second column of Fig. 3. Focusing on the maps generated by HAVF, UOC, and LOT, the shape of land-cover patches (e.g., class C1 and C3 at the image center area) is more similar to that in the reference image than for the DH results, although there are slightly more speckled artifacts. UOS produces the most speckle artifacts. Compared with UOS, HAVF, UOC, and LOT, fewer speckle artifacts were generated by the proposed HCPMP algorithm as shown in the last column of Fig. 3. Moreover, HCPMP preserved the structure and shape of patches better than DH. Of the six class-allocation algorithms, HCPMP produced results closest to the reference image in Fig. 2(a) while also creating the most satisfactory land-cover maps, based on visual assessment.

2) Accuracy Assessments: Table II gives the accuracy assessment for the artificial imagery when combining SAM_MSI, ICK_MSI, and MAP_MSI with the six class-allocation algorithms using scale factors 4, 6, and 10. The total number of testing samples (reference subpixels within mixed pixels) was 7120 for the scale factor of 4, and the numbers of testing samples for C_1, C_2, C_3, and C_4 were 2416, 1680, 2807, and 217, respectively. The total number of testing samples was 13 752 for scale factor 6, and the numbers for C_1, C_2, C_3, and C_4 were 4688, 3280, 5374, and 410, respectively. The total number of testing samples was 23 000 for scale factor 10, and the numbers for C_1, C_2, C_3, and C_4 were 8439, 5830, 7901, and 830, respectively. Comparing the OA' for the different scale factors, the accuracy in all cases gradually decreased as the scale factor increased. The reason for this was that the SRM process became more complicated with an increased scale factor, while uncertainty inevitably increased as more spatial locations of subpixels within a coarse mixed pixel needed to be estimated [54]. The accuracies in Table II confirm the above visual assessment. It shows that the accuracies of DH and UOS were significantly lower than those of the other four algorithms, although the accuracy of UOS was higher than that of DH. The accuracy of LOT was slightly higher than those of HAVF and UOC, while HAVF and UOC had almost identical accuracy. The OA' of HCPMP was higher than those of the other five algorithms. Compared with LOT, which had the highest accuracy of the five existing algorithms, HCPMP achieved an average increase of 2.3% using scale factor 4 and about 1.0% increase for scale factors 6 and 10. These improvements were largely due to the fact that auxiliary images were used in the process of class allocation and pure pixels in the auxiliary images provided useful information, thereby increasing the SRM accuracy.

C. Experiment 2: QuickBird Imagery

In this experiment, a 2.44-m multispectral QuickBird image (400×400 pixels) located in the Jiangsu province, China, was used. The QuickBird image shown in Fig. 4(a) contains four main land-cover classes: water, vegetation, buildings, and bare ground, which were considered as endmembers for classification and SRM. Training samples of the four classes were manually chosen from Fig. 4(a) for classification, while the spectral separability of the sample pair of classes was measured by the Jeffries–Matusita distance [16]. The Jeffries–Matusita distance is a widely used measure for evaluating sample quality, and it takes values between 0 (no separability) and 2 (total separability) [16]. Table III shows that spectral separability between classes is very close to the total separability value of 2. Fig. 4(b) shows the reference image that was derived from Fig. 4(a) by a support vector machine (SVM) hard classifier [59]. The OA of the reference image was 94.6% and was evaluated using 500 ground sites in Google Earth. The reference image was transformed to MSIs using the four shifts described in Section IV-A. Using scale factor 4, the MSIs were degraded into coarse fraction images, which were then used as input for the three subpixel sharpening algorithms and the six class-allocation algorithms to recreate land-cover maps with the same spatial resolution as the reference image in Fig. 4(b). The visiting order of classes determined by Moran's I in Table IV was water–vegetation–bare ground–buildings for UOC.

1) SRM Results: Fig. 5 shows the SRM results for the QuickBird image using scale factor 4. It suggests that DH once again produced overly smooth maps and failed to preserve some small patches, especially certain fine linear features (e.g., vegetation inside the buildings in the top left area) when applying SAM_MSI. As shown in the second column of Fig. 5, UOS yielded maps with many speckle artifacts and unsmooth land-cover boundaries. HAVF, UOC, and LOT, on the other hand, performed better than UOS because fewer speckle artifacts were produced. They also recreated small features more accurate than DH. The maps produced by HCPMP were more similar to Fig. 4(b) than those yielded by the other algorithms, especially compared with maps yielded by DH and UOS.

2) Accuracy Assessments: Table V shows the OA' values for the QuickBird image. The total number of testing samples was 28 272, and the testing sample numbers of water, vegetation, buildings, and bare ground were 1746, 8526, 9738, and 8262, respectively. The accuracies in Table II confirmed

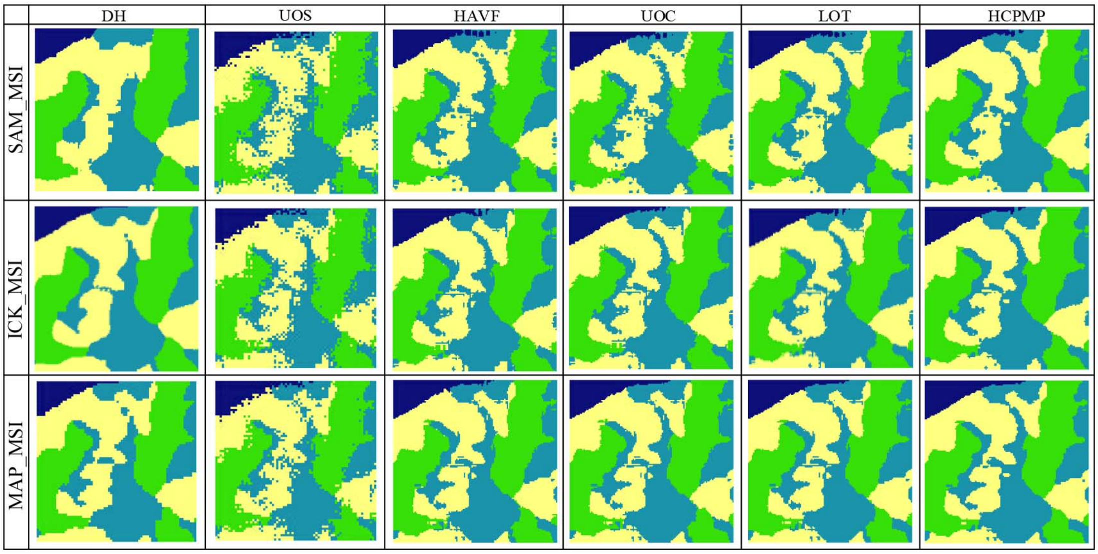

Fig. 3. SRM results for the artificial imagery using scale factor of 10.

TABLE II
ACCURACY (OA′) FOR THE ARTIFICIAL IMAGERY (%)

	S	Class-allocation algorithms					
		DH	UOS	HAVF	UOC	LOT	HCPMP
SAM_MSI	4	83.55	88.12	91.59	91.49	94.19	96.29
	6	81.26	84.90	89.48	89.72	92.98	93.58
	10	78.10	82.34	85.57	84.42	88.90	90.27
ICK_MSI	4	85.18	89.20	94.34	94.38	94.72	96.85
	6	82.29	86.74	93.02	93.41	93.70	94.73
	10	80.46	83.77	87.65	89.15	89.57	90.93
MAP_MSI	4	84.80	89.21	92.75	92.74	93.08	95.83
	6	83.70	87.41	92.18	92.42	92.71	94.07
	10	81.69	84.61	88.40	88.67	89.41	90.59

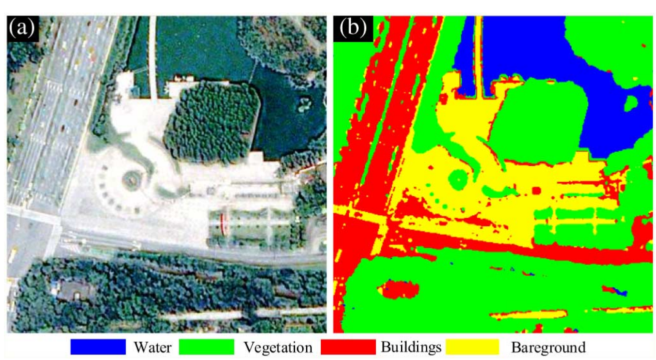

Fig. 4. Experiment on QuickBird imagery. (a) QuickBird imagery. (b) Reference land-cover map generated by hard classification.

the findings in visual assessment. The accuracies of DH and UOS were smaller than those of the other four algorithms, while the accuracies of HAVF, UOC, and LOT presented minor differences, although LOT was slightly more accurate than HAVF and UOC. Compared with LOT, the OA′ of HCPMP had an average improvement of 1.3%. Specifically, HCPMP was 0.89%, 1.24%, and 1.78% more accurate than LOT when combined with SAM_MSI, ICK_MSI, and MAP_MSI, respectively. Additionally, the OA′ of the direct hard classification map from the fraction images of the base-degraded QuickBird image was 67.49%, it was calculated by comparing testing

TABLE III
JEFFRIES–MATUSITA DISTANCE OF FOUR CLASSES IN THE QUICKBIRD IMAGERY

	Water	Vegetation	Buildings	Bare ground
Water	0	1.59	2.00	2.00
Vegetation	1.59	0	1.94	1.99
Buildings	2.00	1.94	0	1.99
Bare ground	2.00	1.99	1.99	0

TABLE IV
MORAN'S I OF FOUR CLASSES IN THE QUICKBIRD IMAGERY ($S = 4$)

Water	Vegetation	Buildings	Bare ground
0.9426	0.8731	0.8253	0.8429

samples with the corresponding sites in the hard classification map. It suggested that SRM results were more accurate than that of hard classification, which was most likely that SRM can address the mixed pixel problem in classification and provide more detailed land-cover of mixed pixels than hard classifiers.

D. Experiment 3: Landsat TM Imagery

A Landsat TM image (800 × 800 pixels) with a spatial resolution of 30 m was used to investigate the performance of the proposed algorithm. The TM image shown in Fig. 6(a) was taken over Maryland, USA, on July 6, 2000, and it covered seven main land-cover classes: buildings, forest, water, bare ground, road, grass, and farmland. The seven classes were considered as endmembers of classification and SRM. Training samples were manually selected from Fig. 6(a). The spectral separability between classes was measured by Jeffries–Matusita distance in Table VI, which revealed that most Jeffries–Matusita distance values were the total separability value of 2. Fig. 6(b) shows the reference image derived from Fig. 6(a) using a SVM hard classifier [59]. The OA of the reference image was 87.6%, evaluated using 1000 ground sites in Google Earth. As before, the reference image in Fig. 6(b) was shifted to MSIs and was degraded into fraction images

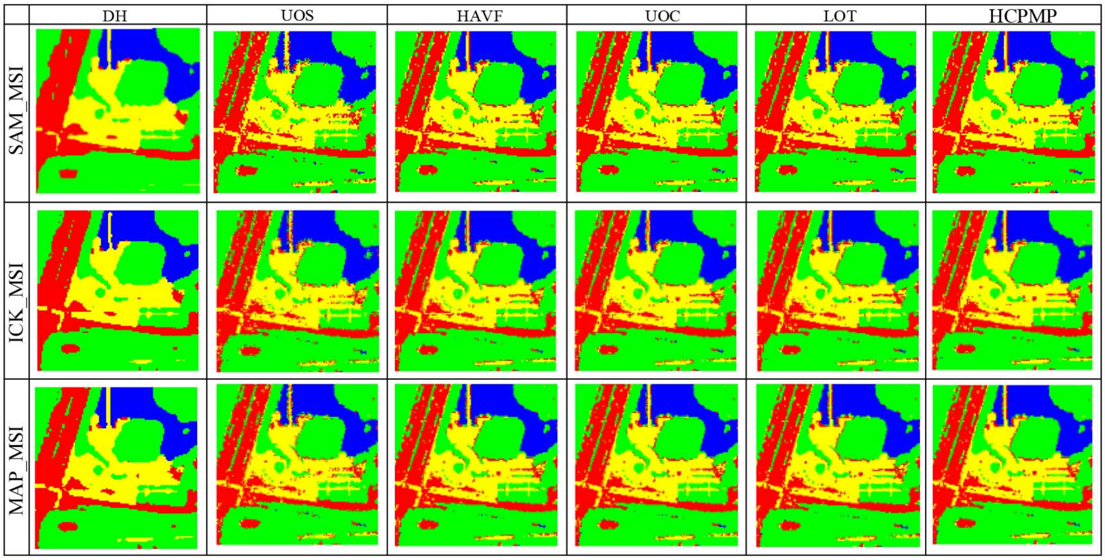

Fig. 5. SRM results for QuickBird imagery using scale factor 4.

TABLE V
ACCURACY (OA') FOR QUICKBIRD IMAGERY(%)

	Class-allocation algorithms					
	DH	UOS	HAVF	UOC	LOT	HCPMP
SAM_MSI	73.93	76.85	84.37	84.06	84.74	85.63
ICK_MSI	74.34	77.44	84.78	84.44	84.88	86.12
MAP_MSI	75.12	77.89	85.20	85.50	85.65	87.43

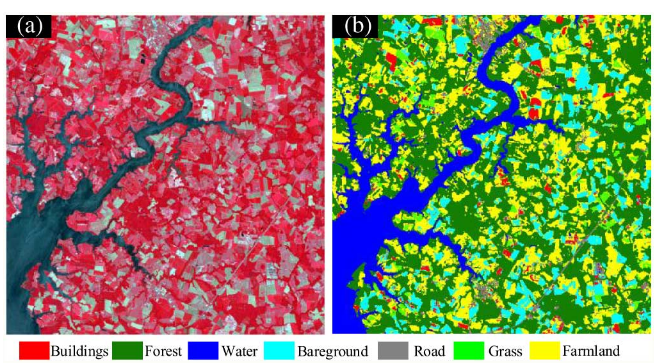

Fig. 6. Experiment on Landsat TM imagery. (a) Landsat TM imagery. (b) Reference land-cover map generated by hard classification from (a).

using scale factor 4. These fraction images were used as input for subpixel sharpening and class allocation. The class visiting order of UOC for the Landsat TM imagery was water–forest–bare ground–farmland–buildings–grass–road, which was determined by Moran's I given in Table VI.

1) SRM Results: SRM maps for the Landsat TM imagery using scale factor 4 are shown in Fig. 7. As indicated in Fig. 7, DH produces overly smooth maps, with many small land-cover patches (e.g., the fine linear roads in the bottom right area of the image) that are not present in Fig. 7(a). Similar to the results in the first two experiments, some speckle artifacts shown in Fig. 7(b) were generated by UOS. HAVF, UOC, and LOT achieved better results than DH and UOS. Focusing on the maps generated by HCPMP, visual assessment shows that the overall performance of HCPMP was very close to the reference image Fig. 6(b).

TABLE VI
JEFFRIES–MATUSITA DISTANCE OF SEVEN CLASSES IN LANDSAT TM IMAGERY

	BD	FR	WT	BG	RD	GS	FD
BD	0	2.00	2.00	1.95	2.00	2.00	1.99
FR	2.00	0	2.00	2.00	2.00	2.00	2.00
WT	2.00	2.00	0	2.00	2.00	2.00	2.00
BG	1.95	2.00	2.00	0	2.00	2.00	2.00
RD	2.00	2.00	2.00	2.00	0	2.00	1.99
GS	2.00	2.00	2.00	2.00	2.00	0	2.00
FD	1.99	2.00	2.00	2.00	1.99	2.00	0

2) Accuracy Assessments: Table VIII presents a quantitative accuracy assessment for the Landsat TM imagery. The total number of testing samples was 267 376, and the testing sample numbers of buildings, forest, water, bare ground, road, grass, and farmland were 9019, 96 486, 14 567, 28 773, 19 284, 11 899, and 87 348, respectively. Similar to the findings in the first two experiments, the performance of DH and UOS was evidently inferior to that of the other four algorithms. There were minor differences in the accuracies of HAVF and UOC, while the accuracy of LOT was slightly higher than those of HAVF and UOC. Compared with LOT, the OA' of HCPMP had an average increase of 1.1%. More precisely, the accuracy of HCPMP was 0.95%, 0.88%, and 1.48% higher than that of LOT when combined with SAM_MSI, ICK_MSI, and MAP_MSI, respectively. In addition, the OA' of the direct hard classification map from the base-degraded TM image was 66.0%, it was also calculated by comparing testing samples with the corresponding sites in the hard classification map. It suggested that SRM results were more accurate than that of hard classification in most cases.

V. DISCUSSION

A. Analysis of the Number of MSIs

Since auxiliary images were important for providing complementary information in SRM, it is worth analyzing the impact of the number of MSIs on the accuracy of SRM. We tested

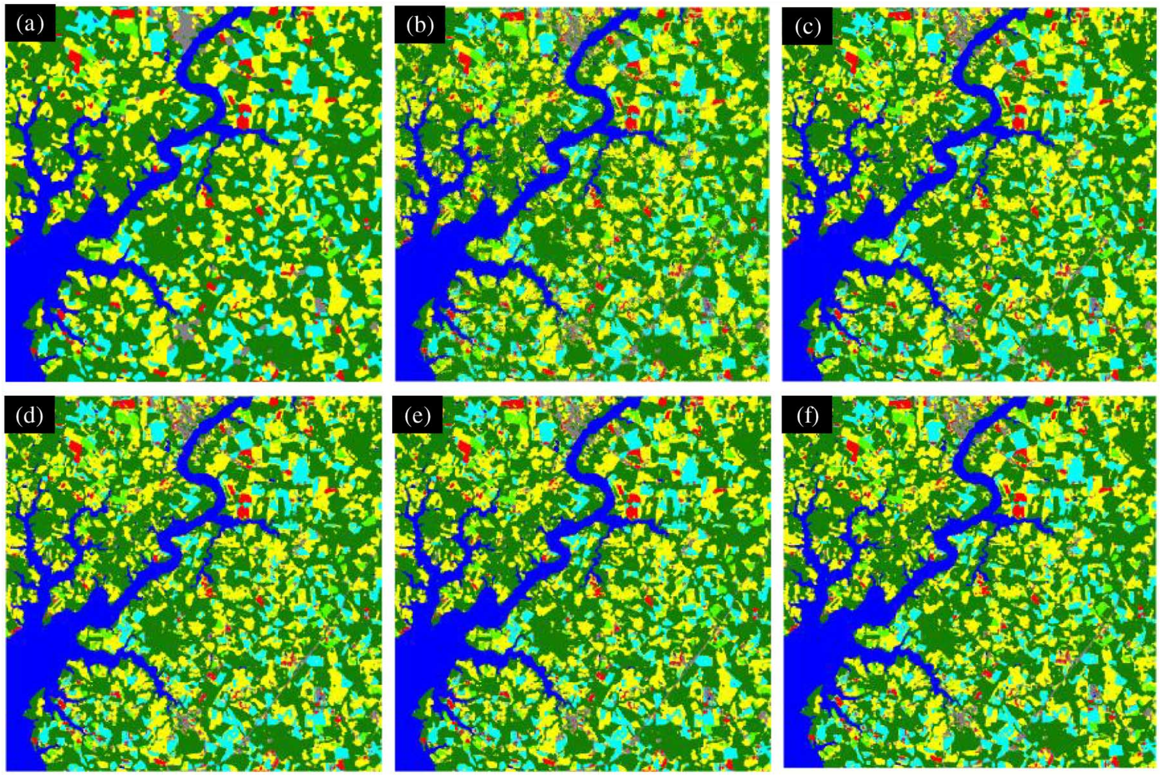

Fig. 7. SRM maps generated by combining ICK_MSI results with class allocation algorithms for Landsat TM imagery using scale factor 4. (a) DH. (b) UOS. (c) HAVF. (d) UOC. (e) LOT. (f) HCPMP.

TABLE VII
MORAN'S I OF SEVEN CLASSES IN SPOT IMAGERY ($S = 4$)

BD	FR	WT	BG	RD	GS	FD
0.6562	0.7411	0.9121	0.7305	0.5584	0.6518	0.6710

BD, buildings; FR, forest; WT, water; BG, bare ground; RD, road; GS, grass; FD, farmland.

four cases of the number of MSIs—1, 3, 5, and 7—on the three experimental images using scale factor 4, with shifts (0,0), $(S/2, 0)$, $(0, S/2)$, $(S/2, S/2)$, $(-S/4, 0)$, $(0, -S/4)$, and $(-S/4, -S/4)$. Fig. 8 shows the accuracy change using different numbers of MSIs for the three experimental images. Fig. 8 confirms the conclusions in [52] and [53], namely, that the accuracy of SRM with auxiliary images is higher than that using only one image (i.e., the base image) and that the accuracy of the six class-allocation algorithms increases with an increase in the number of MSIs. However, the improvement rate of HCPMP was slightly higher than that of the other algorithms, especially for the artificial imagery. This was largely due to the fact that complementary information from auxiliary images was not applied in the existing class-allocation algorithms, whereas HCPMP did use this information. Since HCPMP used a great deal of complementary information to predict the spatial distribution of subpixels, it was slightly more accurate than the five existing algorithms, as shown in Fig. 8.

B. Analysis of Computational Efficiency

Table IX presents the runtime of six class-allocation algorithms on the three experiments. It indicates that DH was the

TABLE VIII
ACCURACY (OA′) FOR LANDSAT TM IMAGERY (%)

	Class-allocation algorithms					
	DH	UOS	HAVF	UOC	LOT	HCPMP
SAM_MSI	63.90	69.72	76.78	74.73	80.19	81.14
ICK_MSI	72.36	74.01	80.27	80.39	81.58	82.46
MAP_MSI	69.09	72.38	76.99	77.13	78.12	79.60

fastest, which is likely due to the fact that this method has the least comparisons of soft attribute values. Similar to the conclusions stated in [54], the runtime of UOS, HAVF, and UOC were very similar, although UOC was more efficient than UOS and HAVF. LOT was the least efficient. Although HCPMP requires more runtime during the first process of allocating classes using pure pixels in auxiliary images, the overall efficiency was increased and it took only slightly less runtime compared with LOT. The reason was that some subpixels assigned to land-cover classes by pure pixels were already removed, and thus, the second process of allocating classes using mixed pixels took less runtime because fewer subpixels needed to be assigned. Additionally, the process of allocating classes to remaining subpixels using coarse mixed pixels could also be done with DH, UOS, HAVF, and UOC. In that case, HCPMP would take less runtime because these four algorithms are more efficient than LOT, as shown in Table IX.

C. Analysis of High- and Low-Resolution Cases

Mixed pixels occur in two different cases: high-resolution (H-resolution) and low-resolution (L-resolution) [6]. The

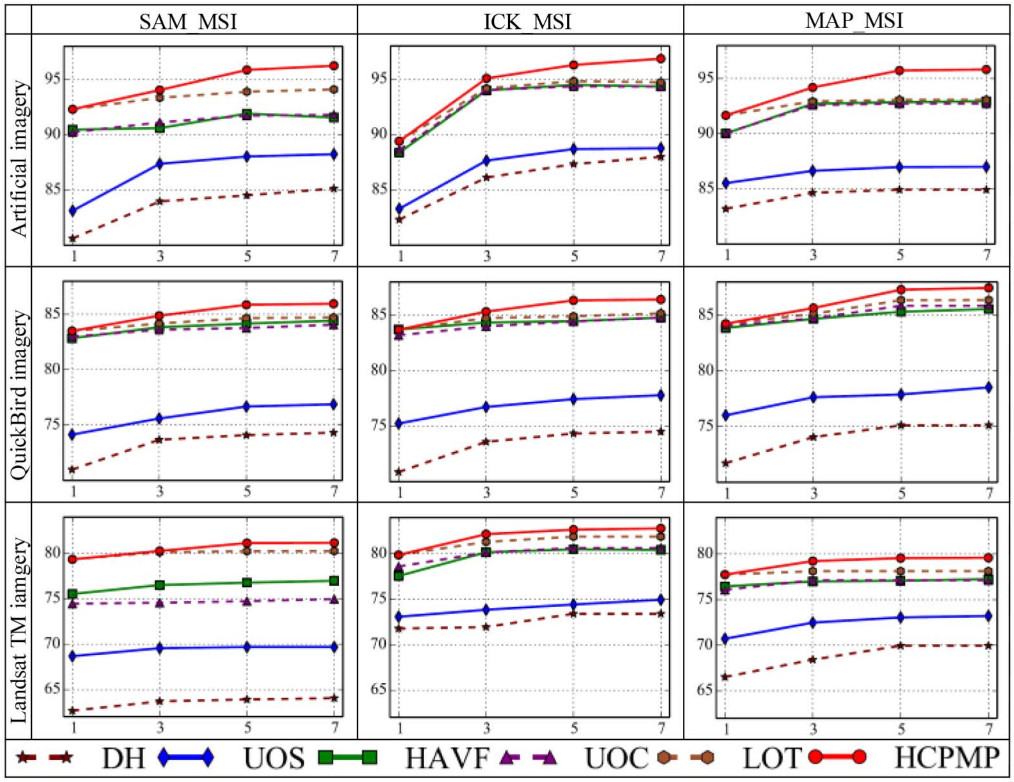

Fig. 8. Impact of the number of MSIs on the accuracy (OA$'$) for the three experiments ($S = 4$).

TABLE IX
RUNTIME OF THE THREE EXPERIMENTS (IN SECONDS)

	Subpixel sharpening	S	Class allocation					
			DH	UOS	HAVF	UOC	LOT	HCPMP
Artificial image	SAM_MSI	4	1.9	3.7	3.8	3.3	9.9	8.9
		6	2.1	5.9	5.9	4.9	12.3	11.2
		10	2.8	8.3	9.2	6.9	18.3	17.3
	ICK_MSI	4	2.2	3.7	3.5	3.4	9.7	8.7
		6	2.1	5.7	5.5	4.5	12.1	11.1
		10	2.9	8.2	8.5	6.3	17.5	16.6
	MAP_MSI	4	1.8	3.7	3.4	3.5	9.6	8.8
		6	2.1	5.7	5.2	4.7	11.9	11.0
		10	2.9	8.2	7.9	6.3	17.3	16.6
QuickBird image	SAM_MSI	4	3.5	7.2	8.3	6.4	19.6	15.9
	ICK_MSI		3.3	7.1	8.1	6.4	19.3	15.1
	MAP_MSI		3.4	7.3	7.2	6.3	19.7	14.9
TM image	SAM_MSI	4	11.6	30.5	33.7	24.4	84.3	79.1
	ICK_MSI		12.7	32.8	30.6	25.5	87.6	81.9
	MAP_MSI		12.6	32.4	29.9	25.1	86.0	79.2

H-resolution case refers to pixels that are smaller than the objects of interest (or large-size contiguous patches), while the L-resolution case refers to pixels that are larger than the objects of interest [6]. HCPMP was performed based on the assumption that there were many pure pixels in auxiliary images. This implies that the study area should be predominated by large-size contiguous land-cover patches (i.e., H-resolution case). In theory, the improvement of HCPMP was caused by pure pixels in auxiliary images of MSIs compared with LOT, which suggests that the fewer the pure pixels in the auxiliary images, the lower the increase of accuracy. In the extreme case, the accuracy of HCPMP would be the same as LOT when there are no pure pixels in the auxiliary images. It can be observed from the reference images in Figs. 2(b), 4(b), and 6(b) that the percentages of H-resolution cases in the artificial image, the QuickBird image, and the Landsat TM image gradually decreased as the complexity of land-cover patches was increased. Tables II, V, and VIII show that, compared with LOT, the OA$'$ of HCPMP (using the scale factor 4) had average increases of 2.3%, 1.3%, and 1.1% for the artificial image, the QuickBird image, and the Landsat image, respectively. Meanwhile, Fig. 8 shows that the accuracy improvement rate of HCPMP gradually reduces with a decrease of H-resolution cases, even though the number of MSIs increases. Specifically, the accuracy improvement rate of HCPMP changed slowly from experiment 1 to experiment 3 when the number of MSIs increased from 1 to 7. Especially, the accuracy improvement rate of HCPMP in the Landsat TM image was the smallest as the number of MSIs increased. This is because the Landsat TM image contained the lowest percentage of H-resolution cases. Therefore, it can be concluded that HCPMP is more suitable in the H-resolution case than in the L-resolution case.

D. Analysis of Different Subpixel Sharpening Algorithms

As the output of subpixel sharpening was a critical input for class allocation, the effect of subpixel sharpening on classification accuracy was also analyzed for the HCPMP algorithm. It can be seen in Tables II, V, and VIII that the results obtained when combining HCPMP with SAM_MSI, ICK_MSI, and MAP_MSI were almost the same for the artificial image. The greatest accuracy for the QuickBird image was produced by combining HCPMP with MAP_MSI, whereas the highest accuracy for the Landsat TM image was generated by combining HCPMP with ICK_MSI. The reason for this was that the different subpixel sharpening algorithms had different characteristics, providing different soft attribute values of subpixels, causing the class-allocation algorithms to achieve different performances for SRM. Although the results from the three different subpixel sharpening algorithms combined with HCPMP were slightly different, the accuracy achieved when combining HCPMP with each of the three subpixel sharpening algorithms was greater and the improvement in OA' was greater than those achieved by other five existing algorithms.

E. Analysis of the Criteria of Defining Pure Pixels

Pure pixels were crucial to improve the performance of HCPMP, because the number of pure pixels in auxiliary images was directly associated with the accuracy improvement. Two criteria were introduced in Section III-A. The first criterion was determined by experts, while the second criterion was calculated according to the given scale factor. In the above three experiments, the threshold was set to $1 - 1/S^2$, because synthetic images free of errors were tested and the pure pixels could be easy to identify by this criterion. However, the threshold used here may not be optimal in case of real remote sensing images or when the scale factor is very large, because errors in soft classification and image registration may be propagated into SRM [6], [23], [55]. The selection of the optimal threshold is a valuable issue when applying real remote sensing images in future research. Remote sensing images in different land surfaces may have different characteristics. Consequently, remote sensing image could be stratified into several subareas according to the geo-detector technique [60], and each subarea might be assigned a different threshold.

F. Impact of Image Registration

The image registration was crucial to SRM with MSIs [37], especially when estimating the shifts between MSIs. For real remote sensing images, many excellent approaches were applied to estimate the shifts between the base image and the auxiliary images in MSIs, such as parametric models [61] and frequency domain algorithms [62]. Although the shifts between real MSIs could be estimated, it was difficult to evaluate the impact of the image registration on SRM [36]. Recently, the impact of image registration on the accuracy of SRM was analyzed with synthetic images [36], [53], [56]. All these studies concluded that the accuracy of SRM with MSIs decreases as the error of image registration increases. Because this study aimed at evaluation of the performance of SRM with MSIs, the shifts between MSIs were assumed to be known, to avoid the error of image registration and shift estimation. Therefore, image registration was beyond the scope of this paper, and it is an interesting issue for analysis of the impact of image registration on the HCPMP when applying real remote sensing images. More information about the impact of image registration on SRM may be found in studies [36], [53], [56].

VI. Conclusion

In this paper, we proposed a new class-allocation algorithm, namely HCPMP, which utilizes auxiliary images in the process of class allocation for STHSRM with MSIs. Complementary information from auxiliary images is commonly used in the first process (subpixel sharpening) of STHSRM with MSIs; however, this information is typically ignored in the second process (class allocation). To make full use of MSIs, HCPMP allocates land-cover classes to subpixels using both the mixed pixels of a base image in MSIs and the pure pixels of auxiliary images in MSIs. As HCPMP uses LOT to determine the land-cover classes of remaining subpixels, it needs slightly longer computing time than DH, UOS, HAVF, and UOC. Still, three experiments showed that HCPMP successfully applies MSIs to produce SRM maps that are visually closer to the reference images and that have greater accuracy than five existing class-allocation algorithms. Especially, it can produce more accurate SRM maps for high-resolution land-cover classes than low-resolution cases. It also takes slightly less runtime than LOT. Hence, HCPMP is an effective solution for applying auxiliary data to the process of class allocation in SRM for remotely sensed imagery.

In HCPMP, complementary information of pure pixels from auxiliary images is applied to the process of class allocation. This paper focused on theoretically evaluating the performances of HCPMP, and synthetic images were only used to avoid the impact of other errors sources (e.g., soft classification and shift estimation). In future research, testing on real MSIs over large areas may be done to analyze whether the advantages of HCPMP as shown here carry through to more realistic real-world situations.

Acknowledgment

The authors would like to thank the editor and anonymous reviewers for their valuable comments and suggestions.

References

[1] G. M. Foody, “Status of land cover classification accuracy assessment,” *Remote Sens. Environ.*, vol. 80, no. 1, pp. 185–201, 2002.
[2] P. Atkinson, M. Cutler, and H. Lewis, “Mapping sub-pixel proportional land cover with AVHRR imagery,” *Int. J. Remote Sens.*, vol. 18, no. 4, pp. 917–935, 1997.
[3] C. E. Woodcock and A. H. Strahler, “The factor of scale in remote sensing,” *Remote Sens. Environ.*, vol. 21, no. 3, pp. 311–332, 1987.
[4] A. J. Tatem, H. G. Lewis, P. M. Atkinson, and M. S. Nixon, “Multiple-class land-cover mapping at the sub-pixel scale using a Hopfield neural network,” *Int. J. Appl. Earth Observ. Geoinf.*, vol. 3, no. 2, pp. 184–190, 2001.
[5] P. M. Atkinson, “Mapping sub-pixel boundaries from remotely sensed images,” in *Innovations in GIS 4*. London: Taylor & Francis, 1997, pp. 166–180.
[6] P. M. Atkinson, “Issues of uncertainty in super-resolution mapping and their implications for the design of an inter-comparison study,” *Int. J. Remote Sens.*, vol. 30, no. 20, pp. 5293–5308, 2009.
[7] A. Tatem, H. Lewis, P. Atkinson, and M. Nixon, “Increasing the spatial resolution of agricultural land cover maps using a Hopfield neural network,” *Int. J. Geogr. Inf. Sci.*, vol. 17, no. 7, pp. 647–672, 2003.
[8] J. Verhoeye and R. De Wulf, “Land cover mapping at sub-pixel scales using linear optimization techniques,” *Remote Sens. Environ.*, vol. 79, no. 1, pp. 96–104, 2002.
[9] K. Mertens, L. Verbeke, E. Ducheyne, and R. De Wulf, “Using genetic algorithms in sub-pixel mapping,” *Int. J. Remote Sens.*, vol. 24, no. 21, pp. 4241–4247, 2003.
[10] P. M. Atkinson, “Sub-pixel target mapping from soft-classified, remotely sensed imagery,” *Photogramm. Eng. Remote Sens.*, vol. 71, no. 7, pp. 839–846, 2005.
[11] L. Wang, Y. Zhang, and J. Li, “BP neural network based subpixel mapping method,” in *Proc. Int. Conf. Intell. Comput.*, 2006, pp. 755–760.
[12] L. P. Zhang, K. Wu, Y. F. Zhong, and P. X. Li, “A new sub-pixel mapping algorithm based on a BP neural network with an observation model,” *Neurocomputing*, vol. 71, no. 10–12, pp. 2046–2054, 2008.

[13] J. P. Ardila, V. A. Tolpekin, W. Bijker, and A. Stein, "Markov-random-field-based super-resolution mapping for identification of urban trees in VHR images," *J. Photogramm. Remote Sens.*, vol. 66, no. 6, pp. 762–775, 2011.

[14] T. Kasetkasem, M. K. Arora, and P. K. Varshney, "Super-resolution land cover mapping using a Markov random field based approach," *Remote Sens. Environ.*, vol. 96, no. 3, pp. 302–314, 2005.

[15] X. Li, Y. Du, and F. Ling, "Spatially adaptive smoothing parameter selection for Markov random field based sub-pixel mapping of remotely sensed images," *Int. J. Remote Sens.*, vol. 33, no. 24, pp. 7886–7901, 2012.

[16] V. A. Tolpekin and A. Stein, "Quantification of the effects of land-cover-class spectral separability on the accuracy of Markov-random-field-based superresolution mapping," *IEEE Trans. Geosci. Remote Sens.*, vol. 47, no. 9, pp. 3283–3297, Sep. 2009.

[17] K. C. Mertens, B. De Baets, L. P. C. Verbeke, and R. R. de Wulf, "A sub-pixel mapping algorithm based on sub-pixel/pixel spatial attraction models," *Int. J. Remote Sens.*, vol. 27, no. 15, pp. 3293–3310, 2006.

[18] Q. Wang, L. Wang, and D. Liu, "Integration of spatial attractions between and within pixels for sub-pixel mapping," *J. Syst. Eng. Electron.*, vol. 23, no. 2, pp. 293–303, 2012.

[19] Y. Chen, Y. Ge, Q. Wang, and Y. Jiang, "A subpixel mapping algorithm combining pixel-level and subpixel-level spatial dependences with binary integer programming," *Remote Sens. Lett.*, vol. 5, no. 10, pp. 902–911, 2014.

[20] Y. Ge, S. Li, and V. C. Lakhan, "Development and testing of a subpixel mapping algorithm," *IEEE Trans. Geosci. Remote Sens.*, vol. 47, no. 7, pp. 2155–2164, Jul. 2009.

[21] Y. Ge, Y. Chen, S. Li, and Y. Jiang, "Vectorial boundary-based sub-pixel mapping method for remote-sensing imagery," *Int. J. Remote Sens.*, vol. 35, no. 5, pp. 1756–1768, 2014.

[22] A. Boucher and P. C. Kyriakidis, "Super-resolution land cover mapping with indicator geostatistics," *Remote Sens. Environ.*, vol. 104, no. 3, pp. 264–282, 2006.

[23] Y. Ge, "Sub-pixel land-cover mapping with improved fraction images upon multiple-point simulation," *Int. J. Appl. Earth Observ. Geoinf.*, vol. 22, no. 1, pp. 115–126, 2013.

[24] Y. F. Zhong and L. P. Zhang, "Remote sensing image subpixel mapping based on adaptive differential evolution," *IEEE Trans. Syst. Man Cybern. B, Cybern.*, vol. 42, no. 5, pp. 1306–1329, Oct. 2012.

[25] Y. F. Zhong and L. P. Zhang, "Sub-pixel mapping based on artificial immune systems for remote sensing imagery," *Pattern Recognit.*, vol. 46, no. 11, pp. 2902–2926, 2013.

[26] X. Xu, Y. Zhong, and L. Zhang, "Adaptive subpixel mapping based on a multiagent system for remote-sensing imagery," *IEEE Trans. Geosci. Remote Sens.*, vol. 52, no. 2, pp. 787–804, Feb. 2014.

[27] Q. Wang, L. Wang, and D. Liu, "Particle swarm optimization-based sub-pixel mapping for remote-sensing imagery," *Int. J. Remote Sens.*, vol. 33, no. 20, pp. 6480–6496, 2012.

[28] Q. Wang, W. Shi, and P. M. Atkinson, "Sub-pixel mapping of remote sensing images based on radial basis function interpolation," *ISPRS J. Photogramm. Remote Sens.*, vol. 92, no. 1, pp. 1–15, 2014.

[29] F. Ling, F. Xiao, Y. Du, H. Xue, and X. Ren, "Waterline mapping at the subpixel scale from remote sensing imagery with high-resolution digital elevation models," *Int. J. Remote Sens.*, vol. 29, no. 6, pp. 1809–1815, 2008.

[30] X. Li, Y. Du, F. Ling, S. Wu, and Q. Feng, "Using a sub-pixel mapping model to improve the accuracy of landscape pattern indices," *Ecol. Indic.*, vol. 11, no. 5, pp. 1160–1170, 2011.

[31] F. Ling, W. Li, Y. Du, and X. Li, "Land cover change mapping at the subpixel scale with different spatial-resolution remotely sensed imagery," *IEEE Geosci. Remote Sens. Lett.*, vol. 8, no. 1, pp. 182–186, Jan. 2011.

[32] F. Ling, X. Li, F. Xiao, S. Fang, and Y. Du, "Object-based sub-pixel mapping of buildings incorporating the prior shape information from remotely sensed imagery," *Int. J. Appl. Earth Observ. Geoinf.*, vol. 18, no. 1, pp. 283–292, 2012.

[33] A. M. Muad and G. M. Foody, "Super-resolution mapping of lakes from imagery with a coarse spatial and fine temporal resolution," *Int. J. Appl. Earth Observ. Geoinf.*, vol. 15, no. 1, pp. 79–91, 2012.

[34] C. Huang, Y. Chen, and J. Wu, "DEM-based modification of pixel-swapping algorithm for enhancing floodplain inundation mapping," *Int. J. Remote Sens.*, vol. 35, no. 1, pp. 365–381, 2014.

[35] Q. Wang, W. Shi, and L. Wang, "Indicator cokriging-based subpixel land cover mapping with shifted images," *IEEE J. Sel. Topics Appl. Earth Observ. Remote Sens.*, vol. 7, no. 1, pp. 327–339, Jan. 2014.

[36] X. Xu, Y. Zhong, L. Zhang, and Z. Hongyan, "Sub-pixel mapping based on a MAP model with multiple shifted hyperspectral imagery," *IEEE J. Sel. Topics Appl. Earth Observ. Remote Sens.*, vol. 6, no. 2, pp. 580–593, Apr. 2013.

[37] F. Ling, Y. Du, F. Xiao, H. Xue, and S. Wu, "Super-resolution land-cover mapping using multiple sub-pixel shifted remotely sensed images," *Int. J. Remote Sens.*, vol. 31, no. 19, pp. 5023–5040, 2010.

[38] J. Hu, Y. Ge, Y. Chen, and D. Li, "Super-resolution land cover mapping based on multiscale spatial regularization," *IEEE J. Sel. Topics Appl. Earth Observ. Remote Sens.*, 2015, doi: 10.1109/JSTARS.2015.2399509, to be published.

[39] A. Boucher, "Sub-pixel mapping of coarse satellite remote sensing images with stochastic simulations from training images," *Math. Geosci.*, vol. 41, no. 3, pp. 265–290, 2009.

[40] X. Li, Y. Du, F. Ling, Q. Feng, and B. Fu, "Superresolution mapping of remotely sensed image based on hopfield neural network with anisotropic spatial dependence model," *IEEE Geosci. Remote Sens. Lett.*, vol. 11, no. 7, pp. 1265–1269, Jul. 2014.

[41] A. J. Tatem, H. G. Lewis, P. M. Atkinson, and M. S. Nixon, "Super-resolution land cover pattern prediction using a Hopfield neural network," *Remote Sens. Environ.*, vol. 79, no. 1, pp. 1–14, 2002.

[42] M. W. Thornton, P. M. Atkinson, and D. A. Holland, "A linearised pixel-swapping method for mapping rural linear land cover features from fine spatial resolution remotely sensed imagery," *Comput. Geosci.*, vol. 33, no. 10, pp. 1261–1272, 2007.

[43] G. M. Foody, "Sharpening fuzzy classification output to refine the representation of sub-pixel land cover distribution," *Int. J. Remote Sens.*, vol. 19, no. 13, pp. 2593–2599, Sep. 1998.

[44] X. Li, F. Ling, Y. Du, and Y. Zhang, "Spatially adaptive superresolution land cover mapping with multispectral and panchromatic images," *IEEE Trans. Geosci. Remote Sens.*, vol. 52, no. 5, pp. 2810–2823, May 2014.

[45] Q. M. Nguyen, P. M. Atkinson, and H. G. Lewis, "Super-resolution mapping using Hopfield Neural Network with panchromatic imagery," *Int. J. Remote Sens.*, vol. 32, no. 21, pp. 6149–6176, 2011.

[46] P. Aplin and P. Atkinson, "Sub-pixel land cover mapping for per-field classification," *Int. J. Remote Sens.*, vol. 22, no. 14, pp. 2853–2858, 2001.

[47] M. Q. Nguyen, P. M. Atkinson, and H. G. Lewis, "Superresolution mapping using a Hopfield neural network with lidar data," *IEEE Geosci. Remote Sens. Lett.*, vol. 2, no. 3, pp. 366–370, Jul. 2005.

[48] M. Q. Nguyen, P. M. Atkinson, and H. G. Lewis, "Superresolution mapping using a hopfield neural network with fused images," *IEEE Trans. Geosci. Remote Sens.*, vol. 44, no. 3, pp. 736–749, Mar. 2006.

[49] Y.-F. Su, G. M. Foody, A. M. Muad, and K.-S. Cheng, "Combining Hopfield neural network and contouring methods to enhance super-resolution mapping," *IEEE J. Sel. Topics Appl. Earth Observ. Remote Sens.*, vol. 5, no. 5, pp. 1403–1417, Oct. 2012.

[50] Y.-F. Su, G. M. Foody, A. M. Muad, and K.-S. Cheng, "Combining pixel swapping and contouring methods to enhance super-resolution mapping," *IEEE J. Sel. Topics Appl. Earth Observ. Remote Sens.*, vol. 5, no. 5, pp. 1428–1437, Oct. 2012.

[51] L. G. Wang and Q. M. Wang, "Subpixel mapping using Markov random field with multiple spectral constraints from subpixel shifted remote sensing images," *IEEE Geosci. Remote Sens. Lett.*, vol. 10, no. 3, pp. 598–602, May 2013.

[52] Q. Wang and W. Shi, "Utilizing multiple subpixel shifted images in subpixel mapping with image interpolation," *IEEE Geosci. Remote Sens. Lett.*, vol. 11, no. 4, pp. 798–802, Sep. 2013.

[53] X. Xu, Y. Zhong, and L. Zhang, "A sub-pixel mapping method based on an attraction model for multiple shifted remotely sensed images," *Neurocomputing*, vol. 134, no. 1, pp. 79–91, 2014.

[54] Q. Wang, W. Shi, and L. Wang, "Allocating classes for soft-then-hard subpixel mapping algorithms in units of class," *IEEE Trans. Geosci. Remote Sens.*, vol. 52, no. 5, pp. 2940–2959, May 2014.

[55] Y. Zhong, Y. Wu, X. Xu, and L. Zhang, "An adaptive subpixel mapping method based on MAP model and class determination strategy for hyperspectral remote sensing imagery," *IEEE Trans. Geosci. Remote Sens.*, vol. 53, no. 3, pp. 1411–1426, Mar. 2015.

[56] Y. Zhong, Y. Wu, L. Zhang, and X. Xu, "Adaptive MAP sub-pixel mapping model based on regularization curve for multiple shifted hyperspectral imagery," *ISPRS J. Photogramm. Remote Sens.*, vol. 96, no. 1, pp. 134–148, 2014.

[57] D. Nigussie, R. Zurita-Milla, and J. G. P. W. Clevers, "Possibilities and limitations of artificial neural networks for subpixel mapping of land cover," *Int. J. Remote Sens.*, vol. 32, no. 22, pp. 7203–7226, 2011.

[58] X. Xu, Y. Zhong, and L. Zhang, "Sub-pixel mapping with multiple shifted remotely sensed images based on attraction model," in *Proc. Int. Conf. Intell. Sci. Intell. Data Eng.*, 2012, vol. 7202, pp. 482–489.

[59] C. C. Chang and C. J. Lin. (2001). *LIBSVM: A Library for Support Vector Machines* [Online]. Available: http://www.csie.ntu.edu.tw/~cjlin/libsvm

[60] J. F. Wang *et al.*, "Geographical detectors-based health risk assessment and its application in the neural tube defects study of the Heshun region, China," *Int. J. Geogr. Inf. Sci.*, vol. 24, no. 1, pp. 107–127, 2010.

[61] L. Zhang, H. Zhang, H. Shen, and P. Li, "A super-resolution reconstruction algorithm for surveillance images," *Signal Process.*, vol. 90, no. 3, pp. 848–859, 2010.

[62] P. Vandewalle, S. Susstrunk, and M. Vetterli, "A frequency domain approach to registration of aliased images with application to super-resolution," *EURASIP J. Appl. Signal Process.*, vol. 2006, no. 71459, pp. 1–14, 2006.

Yuehong Chen received the B.S. degree in geographical information system from Hohai University, Nanjing, China, in 2010, and the M.S. degree in cartography and geographical information system from the University of Chinese Academy of Sciences, Beijing, China, in 2013. He is currently pursuing the Ph.D. degree in cartography and geographical information system at the State Key Laboratory of Resources and Environmental Information System, Institute of Geographical Sciences and Natural Resources Research, University of Chinese Academy of Sciences, Beijing, China.

His research interests include remote sensing image processing and super-resolution mapping.

Yong Ge (M'14) received the Ph.D. degree in cartography and geographical information system from the Chinese Academy of Sciences (CAS), Beijing, China, in 2001.

She is a Professor with the State Key Laboratory of Resources and Environmental Information System, Institute of Geographical Sciences and Natural Resources Research, CAS. She has been involved in the organization of several international conferences and workshops. She has directed research in more than ten national projects. She is the author or coauthor of over 80 scientific papers published in refereed journals, one book, and six chapters in books; she is the editor of one book, and she holds three granted patents in improving the accuracy of information extraction from remotely sensed imagery. Her research interests include spatial data analysis and data quality assessment.

Dr. Ge is a member of the Theory and Methodology Committee of the *Cartography and Geographic Information Society, the International Association of Mathematical Geosciences*, and the Editorial Board of *Spatial Statistics* (Elsevier).

Gerard B. M. Heuvelink received the Ph.D. degree in environmental sciences from Utrecht University, Utrecht, The Netherlands, in 1993.

Since 2003, he has been employed as an Associate Professor of Geostatistics with the Soil Geography and Landscape Group, Wageningen University and as a Senior Researcher Pedometrics and Digital Soil Mapping with ISRIC World Soil Information, since 2011. He is a Visiting Professor at the Institute of Geographical Sciences and Natural Resources Research, Chinese Academy of Sciences, Beijing, China, since 2011. He has authored over 220 scientific publications on geostatistics, spatial uncertainty analysis, and pedometrics, about 90 of which appeared in peer-reviewed international journals.

Dr. Heuvelink is an Associate Editor of *Spatial Statistics* and the *European Journal of Soil Science, and Editorial Board Member of Geoderma, Environmental, and Ecological Statistics, International Journal of Applied Earth Observation and Geoinformation and Geographical Analysis*. In 2014, he was awarded with the Richard Webster Medal of the Pedometrics Commission of the International Union of Soil Science.

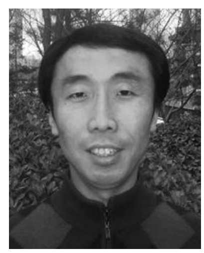

Jianlong Hu received the B.S. degree in information and computing science, and the M.S. degree in computer application technology from Shanxi University, Taiyuan, China, in 2003 and 2006, respectively.

Since 2014, he was a Visiting Scholar with the State Key Laboratory of Resources and Environmental Information System, Institute of Geographical Sciences and Natural Resources Research, Chinese Academy of Sciences, Beijing, China. His research interests include remote sensing image analysis and machine learning.

Yu Jiang received the B.S. degree in geographical information system from Capital Normal University, Beijing, China, in 2012. She is currently pursuing the M.S. degree at the State Key Laboratory of Resources and Environmental Information System, Institute of Geographical Sciences and Natural Resources Research, University of Chinese Academy of Sciences, Beijing, China.

Her research interests include remote sensing image processing and super-resolution mapping.

View publication stats